The Effect of Microchannel Height on the Acoustophoretic Motion of Sub-micron Particles

Tsz Wai Lai[1], Thilhara Tennakoon[1], Ka Chung Chan[1], Chun-Ho Liu[2], and Christopher Yu Hang Chao[1,3], Sau Chung Fu[1,*]

[1] Department of Building Environment and Energy Engineering, The Hong Kong Polytechnic University, Hong Kong, China.

[2] Department of Mechanical Engineering, The University of Hong Kong, Hong Kong, China

[3] Department of Mechanical Engineering, The Hong Kong Polytechnic University, Hong Kong, China.

[*] Corresponding author: schung.fu@polyu.edu.hk

Contact details of the corresponding author:

Postal Address: The Hong Kong Polytechnic University, Kowloon, Hong Kong, China

Telephone number: 27664858

Abstract

Acoustophoresis is an effective technique for particle manipulation. Acoustic radiation force scales with particle volume, enabling size separation. Yet, isolating sub-micron particles remains a challenge due to the acoustic streaming effect (ASE). While some studies confirmed the focusing ability of ASE, others reported continuous stirring effects. To investigate the parameters that influence ASE-induced particle motion in a microchannel, this study examined the effect of microchannel height and particle size. We employed standing surface acoustic wave (SSAW) to manipulate polystyrene particles suspended in the water-filled microchannel. The results show that ASE can direct particles as small as 0.31 μm in diameter to the centre of the streaming vortices, and increasing the channel height enhances the focusing effect. Smaller particles circulate in the streaming vortices continuously, with no movement towards the centres. We also discovered that when the channel height is at least 0.75 the fluid wavelength, particles transitioning from acoustic radiation-dominated to ASE-dominated share the same equilibrium position, which differs from the pressure nodes and the vortices' centres. The spatial distance between particles in different categories can lead to particle separation. Therefore, ASE is a potential alternative mechanism for sub-micron particle sorting when the channel height is accurately adjusted.

Keywords:

Microfluidics, Acoustophoresis, Acoustic streaming, Particle concentration, Sub-micron particle separation,

1. Introduction

The combination of acoustics and microfluidics can perform microorganism separation accurately and quickly [1-4]. Being label-free and biocompatible, acoustophoretic separation has been applied to many biological and biomedical processes, including separation of blood

components, stem cell extraction, and cancer cell isolation [5-7]. Most acoustofluidic separation devices generate an acoustic field inside a fluid-filled microchannel and use acoustic radiation force (ARF) to control the particle's trajectory [4-10]. In a standing acoustic field, ARF drives particles with a positive acoustic contrast factor (ACF), a parameter that considers the compressibility and density of the particles and the fluid medium, to the pressure nodes. Since ARF scales with particle volume, larger particles experience stronger ARF, enabling them to reach the pressure node sooner [11]. Petersson et al. [12] utilized this time difference to concurrently sort polystyrene particles ranging from 2 µm to 10 µm.

In addition to ARF, particles in an acoustic field experience the Stokes drag force induced by the acoustic streaming effect (ASE), which is the secondary effect of wave propagation [13-16]. The Stokes drag force is proportional to the particle's diameter [17]. For small particles, the drag force induced by ASE overcomes ARF and drives the particles into the circular streamlines [18-19], posing a lower size limit on ARF-driven separation. Thus, suppressing ASE became a common goal to improve the handling of nanoparticles [20-23].

However, under certain circumstances, ASE can indeed facilitate useful applications, not only mixing of fluids but also particle concentration. Li et al. [24] and Shilton et al. [25] demonstrated the rapid concentration of particles by surface acoustic waves (SAW) in a microliter water drop. The propagation of SAW generates an azimuthal bulk recirculation around the vertical axis in the microdrop, whereby particles can concentrate at the centre of the droplet. Li et al. [24] explained the inward radial force by the shear difference between the outer radius and the centre of the droplet. Particles diffuse from the high shear region at the outer radius towards the low shear region at the centre. The strength of this shear-induced concentration effect reduces as the particle size goes down. Collins et al. [26-28] employed that size dependence to separate micron particles. In their traveling SAW (TSAW) device, SAW propagates orthogonally to the lateral flow, forming vortices with a vertical axis of rotation

inside the microchannel. The streaming flow directs particles of all studied sizes into the vortical flow. Among them, 2 μm-particle suspensions are captured in the vortex centre, while 1 μm particles are small enough to escape being trapped [28]. Due to the limited capacity at the vortex centre, 2 μm particles are alternately captured and released. To achieve continuous particle focusing using ASE, Antfolk et al. [29] employed a two-dimensional acoustic wave to produce a large rotational flow in the microchannel, enabling particles as small as 0.5 μm to concentrate at the centre. Since the axis of rotation is parallel to the lateral flow, the focused particles can move along the flow.

Yet, the concentration process is highly dependent on the applied power [24], which has a positive correlation with the streaming velocity [25], not too high nor too low. On one hand the weak flow at low power is insufficient to drive particles, but on the other hand, in the strong convection at high power, the inertia of particle dominates over the shear gradient and moves them away from the centre, causing particle dispersion [30]. As can be found in spiral microchannels, fluid moving in a circular path introduces a centrifugal acceleration directed radially outward [31-32], which increases with the flow velocity [33]. Therefore, the competition between the inward and outward radial motions is associated with the streaming velocity [24]. When the streaming velocity is above a critical value, the inertia force experienced by the particles is no longer negligible and counterbalances the force induced by shear gradient.

Besides the streaming velocity, particle size and excitation frequency also play an important role on the particle motion [30]. In a streaming vortex, small particles, whose inertia force is insignificant, are dominated by the shear gradient and tend to concentrate at the centre. The influence of the inertia force increases with the particle size. When the particle size is above a critical value, the inertia force is sufficient to cause an outward particle motion [34]. Particles then reach their equilibrium radial position where the opposite forces contribute

equally to the particle motion. There, they circulate in a particular vortex line without further radial movement [34]. A higher excitation frequency would reduce the critical particle size [30]. The shear-induced inward motion and inertia-induced outward motion are two different mechanisms that affect the behaviour of small particles circulating in streaming vortices significantly.

To enhance the application of these mechanisms on small particle manipulation, one must be able to control the streaming vortices, both the streaming velocity and the streaming pattern. These parameters are associated with the interaction between the fluid and the boundary confining it [35-37], especially in SAW devices [38]. SAW streaming is caused by wave attenuation in fluid [39]. In TSAW devices, SAW with a wavelength of λ_{SAW} reaching the solid-fluid interface radiates a longitudinal wave with a wavelength of λ_f into the fluid [40-41]. Due to the different sound velocities of the mediums, the longitudinal wave is diffracted by an angle, also known as the Rayleigh angle [42]. A body force is generated on the fluid in the direction of wave propagation [43-44]. Once the fluid steam reaches the channel ceiling, a reverse flow is induced, leading to streaming rolls near the channel wall [41]. Several numerical studies have shown that the streaming rolls are larger and stronger in higher channels [38, 45-46]. Devendran et al. [45] explained that, as the channel height (h) increases, the acoustic wave attenuates more, increasing the effect of streaming. In very high channels, the streaming rolls do not continue to grow but significantly weaker counter vortices would appear in the upper section since the excitation is from the bottom [46]. In contrast, in very short microchannels ($h = 0.25\ \lambda_f$), the streaming field is dominated by the displacement conditions along the substrate, forming small periodic streaming vortices with decreasing strength as SAW dissipates [38].

In another branch of SAW devices, the standing SAW (SSAW) devices, where the fluid inside the microchannel is excited by a standing wave produced by the wave interference of two SAWs propagating in opposite directions, the streaming field is often described as periodic

vortices with equal size and strength along the substrate. However, this description is only true for microchannels with a channel width less than λ_{SAW} [45]. As energy is transferred from solid to fluid, the amplitude of SAW reduces, resulting in a mismatch in the amplitude of the opposite propagating SAWs. Devendran et al. [45] suggested to consider a travelling wave component near the channel walls when using microchannels wider than λ_{SAW}. Therefore, the microchannel should be divided into two regions, the near wall region with large streaming rolls and the centre region with periodic vortices. *h* changes the streaming field in the same way as in TSAW devices.

The microchannel's cross-section directly affects the streaming velocity and streaming pattern [31-33]. Consequently, the ASE-driven particle motion can be manipulated by changing the channel's geometry. In this study, we experimentally investigated the effect of *h* on the movement of sub-micron particles, which are often dominated by ASE, and evaluated how the streaming velocity and streaming pattern change with *h*. To obtain a detailed size dependence of ASE-driven particle motion, we examined the motion of polystyrene particles with diameters of 0.31 µm, 0.38 µm, 0.49 µm, 0.79 µm, 1.1 µm, and 5 µm. In addition to shear-induced focusing, we discovered an alternative focusing mechanism induced by the particle inertia, that directs particles radially outward and detaches them from the streaming vortices to an equilibrium point. The spatial distance between them and the particles concentrated at the vortex centre by the shear gradient can potentially lead to a new separation strategy for sub-micron particles. Surprisingly, *h* can serve as a parameter for controlling the threshold between the two ASE-induced focusing mechanisms.

2. Materials and methods

2.1 Working mechanism

This study employs SSAW devices, in which the acoustic field used for particle manipulation is generated by two counter-propagating SAWs. Figure 1a shows the schematic

diagram of the SSAW device. On a piezoelectric substrate, conventional interdigital transducers (IDTs) are fabricated on both sides of the microchannel at equal distance. The IDTs are connected to the signal generator, which supplies a sinusoidal electric signal, to produce SAWs that travel towards the microchannel. The wavelength of SAW on the solid substrate is λ_{SAW}, while the wavelength of the longitudinal wave radiated into the fluid is λ_f, which can be calculated by the excitation frequency and the speed of sound in the fluid medium. The studied microchannels have a constant width of $2\lambda_{SAW}$, but h is different multiples of λ_f, namely $0.25\lambda_f$, $0.5\lambda_f$, $0.75\lambda_f$, and λ_f. We identify the devices according to h as Devices 1 ($0.25\lambda_f$) to 4 (λ_f). The microchannels are made of polydimethylsiloxane (PDMS), and water is the fluid medium carrying particle suspensions through the acoustic region. The reflection of acoustic waves at the PDMS-water boundaries, calculated by the difference in acoustic impedance between the materials, is negligible since PDMS and water have similar acoustic impedance [47].

Figure 1b shows the coordinate system used in this study. We assumed that the acoustophoretic effect, which takes place in the xy-plane, is independent of the lateral flow. Under acoustic excitation, the most common acoustic forces affecting particle suspensions are the ARF $\boldsymbol{F_r}$, depending on the ACF $\phi(\beta,\rho)$, and the Stokes drag $\boldsymbol{F_d}$. In a half-wavelength standing plane wave, $\boldsymbol{F_r}$ and $\boldsymbol{F_d}$ can be written as [48]:

$$\boldsymbol{F_r} = -\left(\frac{\pi p_0^2 V_p \beta_f}{2\lambda}\right)\phi(\beta,\rho)\sin\left(\frac{4\pi l}{\lambda}\right) \tag{1}$$

$$\phi(\beta,\rho) = \frac{5\rho_p - 2\rho_f}{2\rho_p + \rho_f} - \frac{\beta_p}{\beta_f} \tag{2}$$

$$\boldsymbol{F_d} = 6\pi\mu r\boldsymbol{v} \tag{3}$$

where λ is the wavelength of the standing wave, p_0 is the acoustic pressure, V_p is the particles' volume, β and ρ are the compressibility and density (the subscripts p and f refer to the particles and fluid medium, respectively), l is the distance from a pressure node, μ is the dynamic

viscosity of the fluid, r is the particle radius, and $\boldsymbol{v}$ is the particle velocity relative to the ASE-induced streaming flow. In Equation (1), $\boldsymbol{F_r}$ has a sinusoidal distribution over the half wavelength interval, indicating that the ARF equals zero at pressure nodes and antinodes. The force-balance point of a particle depends on the sign of ACF [48].

The equations show that $\boldsymbol{F_r}$, which scales with r^3, is the dominant force for large particles, but $\boldsymbol{F_d}$, which scales with r, becomes significant when the particle size decreases. Once the particles are driven into the streaming vortices, they circulate and experience the inward radial force induced by the shear gradient. When the streaming velocity is sufficiently large or the particle size is above a critical value, the inertia of particle will drive particles radially outward.

(a) (b)

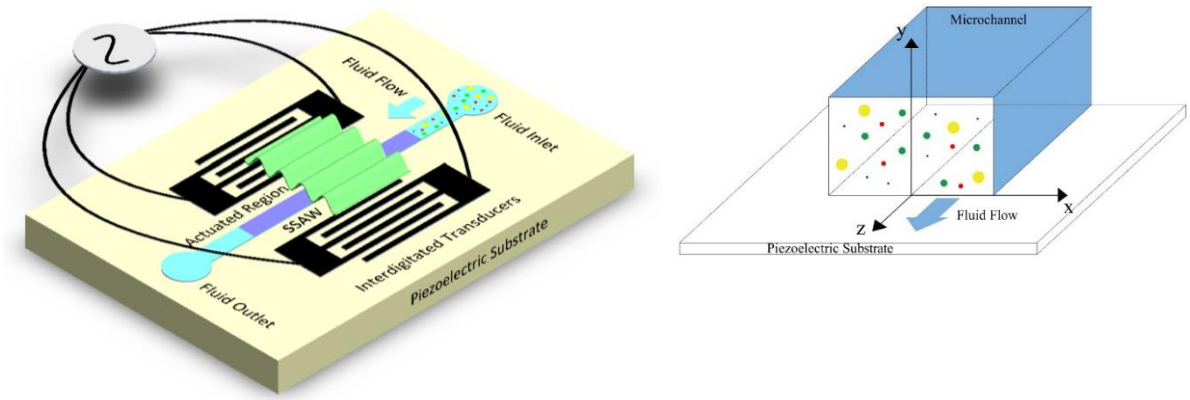

Figure 1: (a) The schematic diagram of SSAW devices. (b) The coordinate system employed in this study.

2.2 Device fabrication

To avoid the misalignment issues that appear in the conventional SSAW devices, this study employed self-aligned IDTs [49], where the IDTs and microchannel were fabricated simultaneously. Figure 2 shows the fabrication process. First, we designed the photomask for the microchannel, on which the IDTs' patterns were also printed. Each IDT has 20 electrodes. The width of the electrodes and the space between them are 50 μm, i.e., the designed λ_{SAW} is

200 µm. Next, we followed the photolithography procedures to construct the microchannel master mold. Silicon wafers were coated with negative photoresist SU-8 2050 (Kayaku Advanced Materials, USA) by a spin coater (WS-650-23, Laurell Technologies, USA). We controlled the spinning speed to achieve the required photoresist thickness on separate wafers. The spin-coated wafers were then soft baked using a programmable digital hotplate (HP40A EchoTherm, Torrey Pines Scientific, USA) for 1 minute at 65°C, followed by several minutes at 95°C depending on the photoresist thickness. Afterwards, the wafers covered with the photomask were subject to UV exposure (ABM, USA) and post-exposure baking. The unexposed photoresist was dissolved in the SU-8 developer (Kayaku Advanced Materials, USA) following the immersion development process. The height of the microchannel master was confirmed using an optical profilometer (DektakXT, Bruker, USA). Finally, trichloro(1H,1H,2H,2H-perfluorooctyl)silane (Sigma-Aldrich, USA) was deposited on the master via evaporation to ensure the easy detachment of the cured PDMS produced later.

The soft lithography process began with the PDMS prepolymer and the cross-linking curing agent (Sylgard 184, Dow Corning, USA) mixed in a 10:1 ratio. The mixture was cast on the microchannel molds, degassed in a vacuum desiccator (Bel-Art - SP Scienceware, USA), and cured at 80°C in an oven (UF110, Memmert, Germany). Then, the PDMS microchannels were detached from the molds and bonded onto 128° y-cut lithium niobate substrates (OST Photonics, China) using a plasma cleaner (ZEPTO W6, Diener, Germany). The IDTs were completed by filling the IDTs' patterns with gallium indium eutectic (Sigma-Aldrich, USA). Thus, alignment was automatically accomplished. With the thickness of the IDTs changing with h, we measured the frequency response of the devices to evaluate their performance (see Figure 3a). As the differences were minor, we considered that the generated signal was independent of the IDT thickness. Since all the devices peaked at approximately 18.4 MHz, we

chose that to be the excitation frequency. As the speed of sound in water at 20℃ is 1481 m/s, λ_f is ~80 µm.

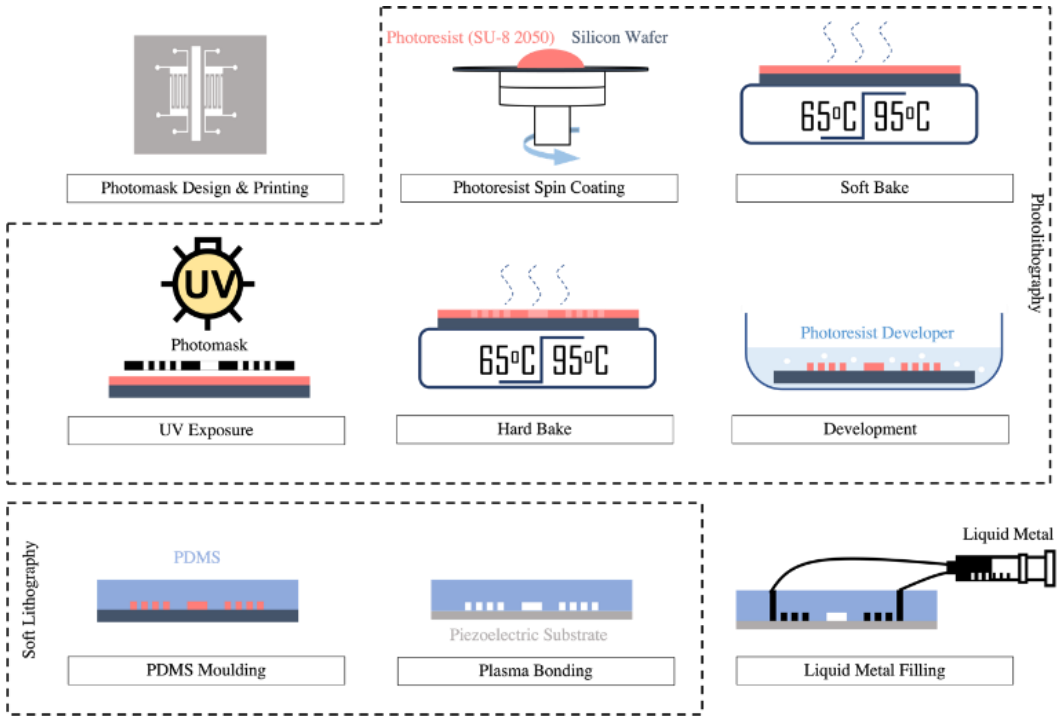

Figure 2: Fabrication process of the self-aligned IDT devices.

2.3 Experimental setup

Figure 3b shows the experimental setup. The self-aligned IDTs were connected to a function generator (AFG3152C, Tektronix, USA), which supplied a sinusoidal wave with an amplitude of 5V. Fluorescent polystyrene particles (Fluoro-max dyed aqueous fluorescent particles, Thermo Fisher Scientific, USA) with a density of 1.05g/cm^3 were suspended in water at a mass concentration of 0.01% and stored in a 0.1 ml microliter syringe (Rongtai Biochemical, China). The flowrate was controlled by a syringe pump (LSP02-2B, Longer Precision Pump, China). The SSAW devices were placed on the stage of an upright optical microscope (ECLIPSE Ni-E, Nikon, Japan), facilitating the observation of the particle movement from the top. In other words, the particle movement in the xz-plane was recorded by the camera, while the y-position of the particles was estimated by the position of the

microscope stage. For each device, the experiment was conducted twice to ensure the repeatability of the particle motion.

(a)

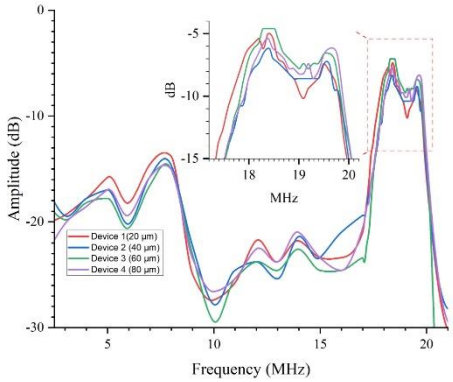

(b)

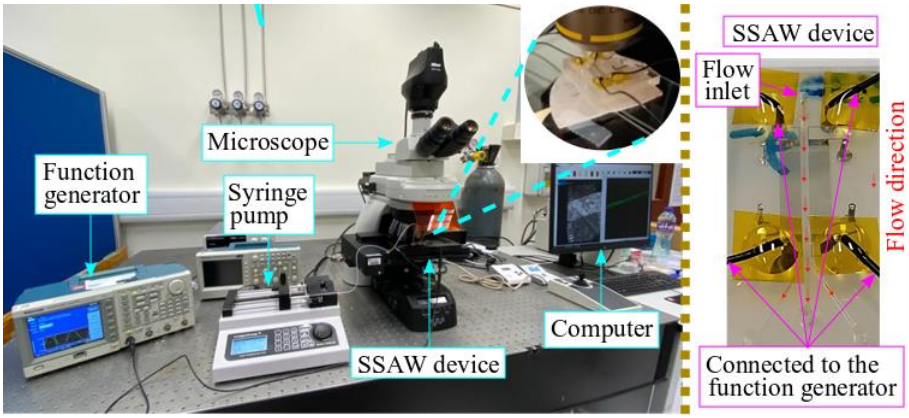

Figure 3: (a) Frequency response of Devices 1 to 4. (b) The experimental setup. The device was placed on the stage of the microscope. The inset image shows the device on the stage. The right image shows the device on which the red arrows indicate the flow direction.

3. Results and discussion

3.1 The pressure node positions

In an acoustic field, large polystyrene particles are driven towards the pressure nodes by ARF. 5 μm particles are considered large enough to be dominated by ARF, allowing their

locations to represent the pressure nodes. Moreover, these particles move sidewise to the pressure nodes without rotational motion, indicating that they are not disturbed by ASE.

The results indicate that *h* affects the pressure node positions. Table 1 shows the x-position of the pressure nodes in Devices 1 to 4. In SSAW devices, the acoustic wave has a standing wave pattern horizontally but propagates upwards [50]. The pressure field has only vertical pressure nodes in very thin microchannels ($h < 0.5\lambda_f$), while it contains horizontal pressure nodes (HPNs) as *h* increases leading to particles' vertical migration [51]. In Device 1 ($h < 0.5\lambda_f$), the pressure nodes, which are ~ $0.5\lambda_{SAW}$ apart, are associated with the displacement conditions along the substrate. The results reveal that SSAW on the substrate has a pressure antinode at the centre of the channel (x = 0), and the actual wavelength is ~201µm (~1µm different from the initial design). As *h* increases, a HPN should appear in Device 2 and two HPNs in Devices 3 and 4. Thus, when $h \geq 0.5\lambda_f$, particles' final position can no longer be predicted by the pressure nodes of SSAW on the substrate.

Table 1: X-position of the 5 µm Particles.

Device no.	Channel height (*h*)	x-position of the 5 µm particles (µm)				
1	$0.25\lambda_f$	±52	±149			
2	$0.5\lambda_f$	0	±25	±62	±150	±185
3	$0.75\lambda_f$	0	±60	±135	±185	
4	λ_f	0	±60	±127	±177	

3.2 The acoustic streaming vortices

The movement of small particles, such as 0.31 µm, is dominated by the Stokes drag force. In our experiment, we observed that 0.31 µm particles were in swirling motion shortly after switching on the acoustic excitation. The particles then moved into the streaming vortices. In all devices, a row of eight streaming vortices appeared with the axis of rotation parallel to the flow direction. *h* affects the position and size of the vortices. The vortex patterns from the four devices are grouped into two variations for the thin and thick microchannels. Figure 4

shows the schematic diagram of the vortex patterns in the cross-sectional view of the microchannel. The direction of the vortices is determined by focusing the microscope on two separate layers and recording the particle movement in the x-direction of both layers. The vertical direction is added afterward to complete the streaming flow. Since the pattern is always left-right symmetric, we refer to vortices from the centre to the sidewalls as V1 to V4. Supplementary Video 1 shows the vortex patterns obtained from thin (Device 1) and thick (Device 3) microchannels.

In thin microchannels (Device 1), the streaming vortices appeared in pairs. The streaming field is believed to be dominated by the displacement condition along the substrate [38], where the adjacent vortices were initiated at the pressure node and circulated in opposite directions. Although the channel width is larger than λ_{SAW}, the streaming rolls caused by the travelling wave component of SSAW near the channel walls did not appear, indicating that wave attenuation is insignificant when h is short. The vortices along the channel width have nearly constant size.

In thick microchannels (Devices 2 to 4), the streaming vortices moved apart from each other. V1 moved closer to x = 0, while V4 moved towards the sidewalls. In terms of size, V2 and V3 became clearly larger than V1 and V4. Here, we believed V3 is the large streaming rolls caused by the travelling wave component of SSAW. As the longitudinal wave propagated at Rayleigh angle (~23º in water [43]), V3 was at some distance from the wall, inducing counter rotating V4. However, the size of V4 is restricted by the space. For V1 and V2, they should be driven by the standing component of SSAW. The reason for V1 being smaller can be associated with the amplitude of SSAW, which is the smallest at the centre of the microchannel. Furthermore, V2 is next to the strong streaming roll V3, which may have a strengthening effect and increase the size of V2.

The number of vortices depends on the channel's geometry. When the channel height is less than $0.5\lambda_f$ or the width is less than λ_{SAW}, the number of vortices can be determined by the number of λ_{SAW} included in the channel width, in which one λ_{SAW} contains four vortices [50]. Otherwise, the travelling wave component of the SSAW on the substrate would produce large streaming rolls near the channel walls [45], which may be significantly large and occupy a length of several λ_{SAW}, leading to a reduced number of streaming vortices.

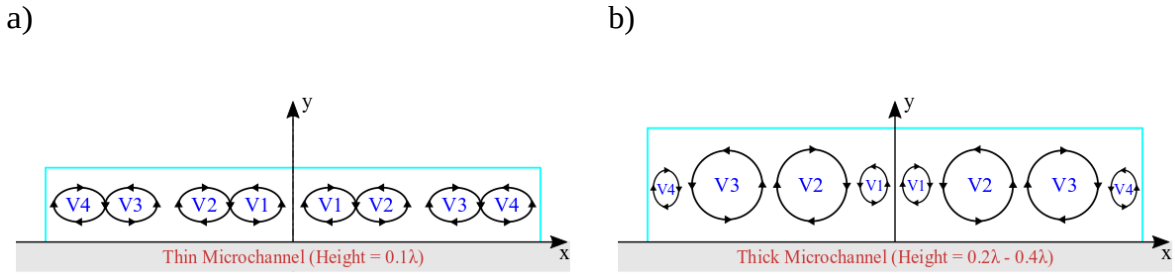

Figure 4: Schematic diagrams of the streaming pattern in the cross-sectional view of a) thin (Device 1), and b) thick (Devices 2-4) microchannels. The streaming vortices are identified as V1 to V4 from the y-axis to sidewalls.

3.3 The ASE-induced focusing effect caused by the shear gradient

In a thin microchannel (Device 1), the shear-induced focusing did not occur. 0.31 µm, 0.38 µm, and 0.49 µm particles circulated in the streaming vortex pairs, forming four scattering particle lines whose thickness decreased with particle size (see Figure 5a). On the other hand, 0.79 µm and 1.1 µm particles moved sidewise to the pressure nodes without any rotational motion, indicating that they were driven by ARF.

The focusing effect by shear gradient is dependent on *h*. In the slightly thicker microchannel (Device 2), the shear-induced focusing occurred when the particle size reached 0.49 µm. The smaller particles (0.31 µm and 0.38 µm) were driven in V1 to V3, but neither had the correct strength to facilitate the focusing effect (see Figure 5b). Particles scattered in V1 and V3, while they stayed on the outer radius of V2. According to Li et al. [24], the streaming velocity in V2 was larger than in V1 and V3, causing the particle inertia to dominate.

For larger particles (0.49 µm and 0.79 µm), some particles accumulated at x = 0, but most concentrated at x = ± 20 µm, ± 86 µm and ± 140 µm. The particle lines at x = ± 20 µm and ± 140 µm were associated with the shear-induced focusing inside V1 and V3 since the inward radial force driving particles to the vortex centre increases with particle size. Although the particle lines at x = ± 86 µm were near V2, we believed they were caused by another focusing mechanism. 0.49 µm and 0.79 µm particles would experience a stronger inertia force than 0.31 µm and 0.38 µm particles, that is sufficient to detach them from the streaming vortex. This alternative focusing mechanism will be discussed in the next section.

In Device 3, the focusing effect by the shear gradient happened to 0.31 µm, 0.38 µm, and 0.49 µm particles in V1 and V3, whose centres were at x = ± 19 µm and ± 139 µm, respectively (see Figure 5c). The results indicate that the focusing strength of V1 and V3 increased from Device 2 to Device 3 where the shear gradient in Device 3 was adequate to concentrate also the 0.31 µm and 0.38 µm particles. Interestingly, the streaming field among V1 to V3 varied in the same way as in Device 2, i.e., particles in V1 and V3 are dominated by the shear gradient while particles in V2 are dominated by the inertia force.

In the thickest microchannel (Device 4), 0.31 µm, 0.38 µm, 0.49 µm, and 0.79 µm particles concentrated at the centre of V2 and V3 at x = ± 70 µm and ± 120 µm, respectively (see Figure 5d). The results show that the channel height changed the particle-capturing strengths of the streaming vortices.

(a) Device 1

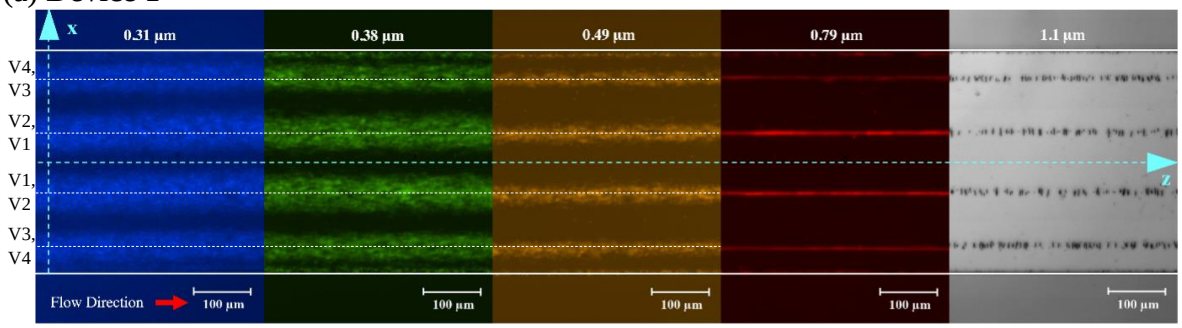

V1 to V4	V1 to V4	V1 to V4	Particles driven by ARF.	Particles driven by ARF.

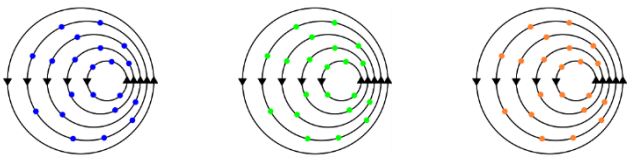

(b) Device 2

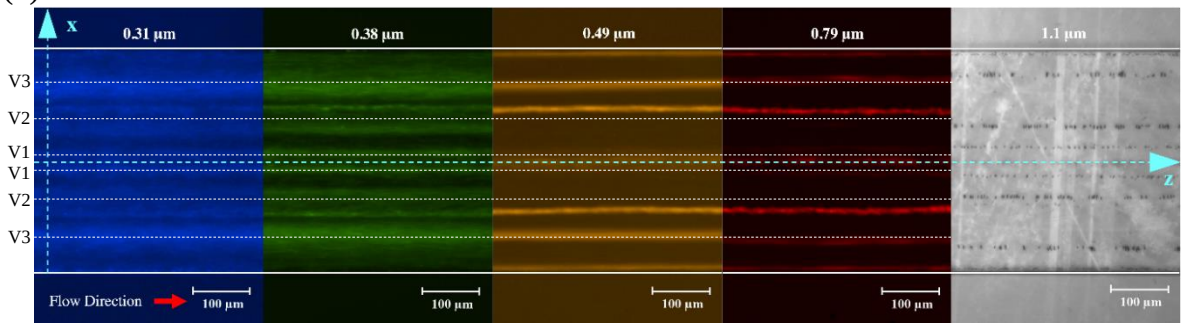

V1 and V3	V1 and V3	V1 and V3	V1 and V3	Particles driven by ARF.

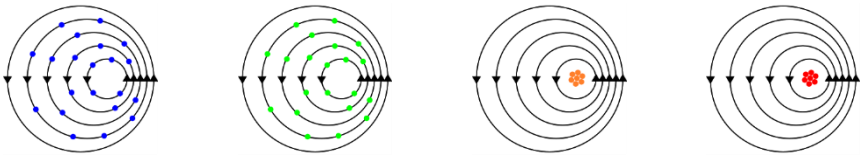

V2	V2	V2	V2

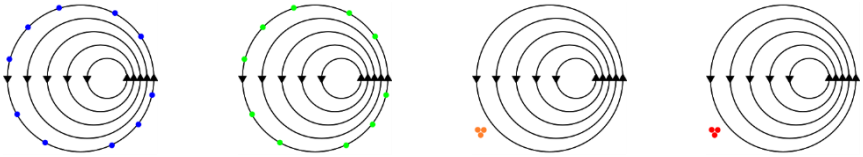

(c) Device 3

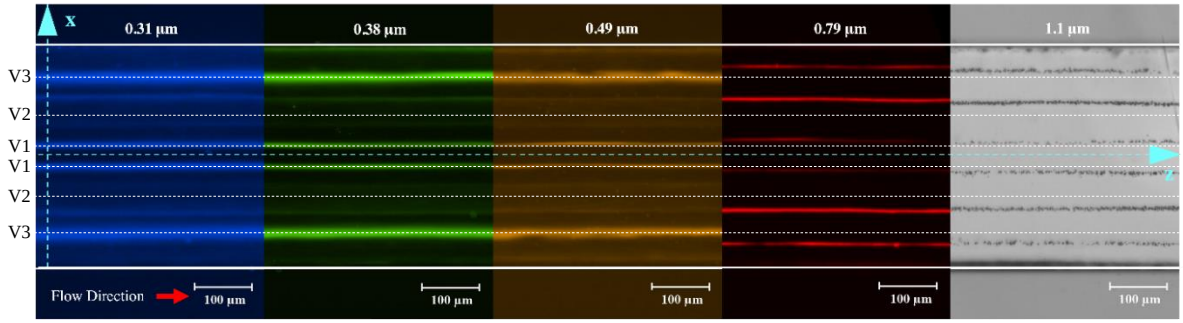

V1 and V3	V1 and V3	V1 and V3	V1 to V3	V1 to V3

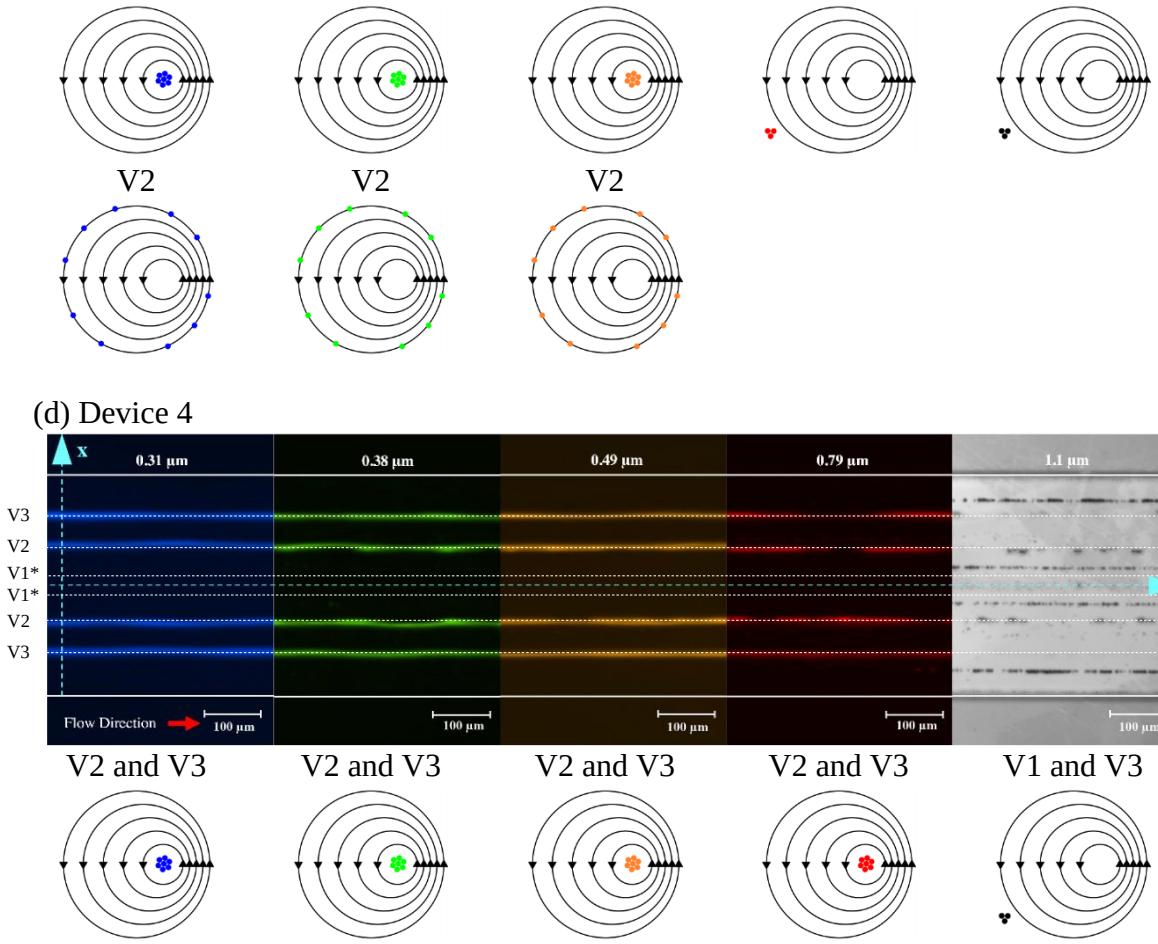

Figure 5: Distribution of 0.31 µm (blue), 0.38 µm (green), 0.49 µm (orange), 0.79 µm (red), and 1.1 µm (black) polystyrene particles in (a) Device 1, (b) Device 2, (c) Device 3, and (d) Device 4. Images show the top view of the microchannels. The flow direction is from left to right (positive z-direction). The channel walls are indicated by the white lines and the scale bar is 100 µm. The white dashed lines indicate the centre of the vortices. In (a), the centrelines of V1/V2 or V3/V4 are very close. In (d), the location of centreline of V1 (V1*) is estimated. The schematic diagrams below each image illustrate the location of the particles within and in the vicinity of streaming vortices.

3.4 The newly discovered ASE-induced focusing effect by the particle inertia

We noticed that some particles, such as the 0.49 μm and 0.79 μm particles in V2 of Device 2, were too small to be driven by ARF but too big to move to the centre of the streaming vortices. The motion of these particles was initiated by the Stokes drag force, which drove them into the vortices. As they circulate, they experience the inertia force that drives them radially outward. In a streaming vortex, the inertia force scales with the particle mass. When the inertia force exceeds a critical value, particles are detached from the vortices. Since all particles in this study have the same density, larger particles experience a stronger inertia force. For instance, in V2 of Device 2, the inertia force on 0.31 μm and 0.38 μm particles can drive them to the outer radius, while the inertia force on 0.49 μm and 0.79 μm particles is large enough to detach the particles. Some of the detached particles get into the adjacent vortices, while others accumulate at specific positions where the streaming velocity is extremely low, i.e., the region between two streaming vortices. In V2 of Device 2, the escaped 0.49 μm and 0.79 μm particles, except those captured by adjacent vortices, arrived at the same places (i.e., $x = \pm 86$ μm), indicating that, for particles in this category, the concentration spots were independent of the particle size (see Figure 5b).

The results obtained from Device 2 show that the occurrence of this focusing effect depends on individual vortices. In the previous section, we show that the streaming velocity varied among the vortices. For Device 2, the velocity of V2 seemed to be higher than V1 and V3, resulting in the newly discovered focusing effect. The flow in V1 and V3 was insufficient to cause noticeable inertia force. Particles were therefore dominated by shear gradient. *h* also affects the focusing effect by inertia. It did not occur in thin microchannels (Device 1). In Device 3, it occurred to 0.79 μm and 1.1 μm particles in V1 to V3, and drove them to $x = \pm 30$ μm, ± 92 μm, and ± 152 μm (see Figure 5c). In Device 4, it occurred only to 1.1 μm particles in V1 and V3, forming particle lines at $x = \pm 32$ μm and ± 150 μm (see Figure 5d). We noticed

that some of the 1.1 μm particles scattered at x = 0 and ± 60 μm, but they were indeed ~34 μm in y-direction above the other particle lines. Nevertheless, they contained only a small portion and therefore are excluded in the following discussion.

3.5 The impact of channel height on particle motion

In our experimental results, it can be observed that the particle motion could be classified in five categories. It is proposed that they can be identified as S1, S2, S3, S4, and S5, with the size in descending order (see Figure 6). Particles in S1 are driven to the pressure node by ARF (insensitive to ASE), while particles in the other categories move into the streaming vortices due to the Stokes drag force. Particles in streaming vortices experience inertia force and shear gradient, leading to particles' radial motion. Particles in S2 and S3 are large enough that the inertia force is significant. The slightly larger S2 particles can detach from the vortex, but S3 particles are held in the rotating flow on the outer radius. For smaller particles, the inertia force becomes negligible. S4 particles are influenced by the shear gradient and concentrate at the vortex centre. However, S5 particles are too small to experience the shear gradient, and thus circulate in the vortex without radial motion. The newly discovered focusing effect by inertia happens to S2 particles, and the shear-induced focusing effect applies to S4 particles.

The sizes of S1, S2, S3, S4, and S5 are variable. Except for S1, the size category that a particle of a given diameter belongs to changes with h (Devices 1 to 4) and the vortex number (V1 to V4). Table 2 shows the classification of the particle diameters from our study into size categories (S1 to S5). Not all size categories appear in a single device, i.e., intermediate size categories may be vacant in some devices. Nevertheless, the trend in particle diameter from S1 to S5 is descending in all devices.

In Device 1, particles behaved similarly in V1 to V4, where they were in either S1 or S5. Thus, both ASE-induced focusing effects were not achievable in thin microchannels ($h = 0.25\lambda_f$). In thicker microchannels (Devices 2 to 4), V4 was not included because it did not

contain particles. In Devices 2 and 3, particles behaved similarly in V1 and V3 but differently in V2. For a given particle size (e.g., 0.49 μm), the inertia force in V1 and V3 was negligible, while in V2 it was large enough to dominate the particle motion, indicating a higher streaming velocity in V2 than in V1 and V3. The growth in *h* (from Devices 2 to 3) increased the streaming velocities of V1 and V3, enabling 0.31 μm and 0.38 μm particles to change their size category from S5 to S4. Additionally, the increased streaming velocity enhanced the particle inertia, causing 0.79 μm particles to change from S4 to S2. However, the streaming velocity in V2 seemed to decrease slightly. The inertia force on 0.49 μm particles reduced, changing them from S2 to S3.

In Device 4, most particles moved into V2 and V3. As *h* increased from Device 3 to 4, the streaming velocity in V2 seemed to decrease further, allowing the 0.79 μm, 0.49 μm, 0.38 μm, and 0.31 μm particles to change to S4. The results indicate that particles in V2 are no longer affected by the particle inertia. Consequently, they are dominated by the shear gradient and concentrate at the vortex centre. Besides, V3 also seemed to decrease slightly. 0.79 μm particles change from S2 to S4 (i.e., from dominated by the particle inertia to dominated by the shear gradient). Yet, the impact on V1 was unclear as all particles moved away.

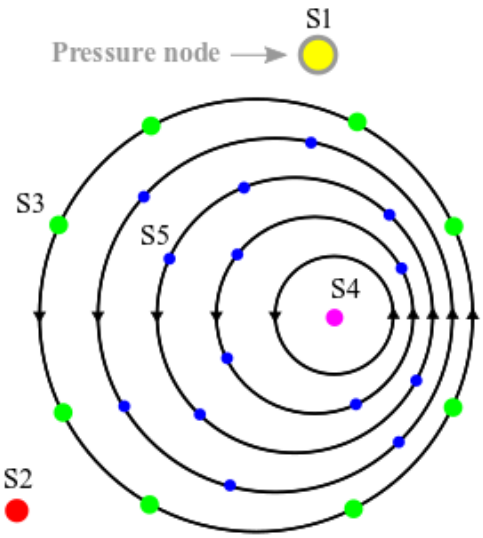

Figure 6: Schematic diagram showing the position of the size categories (S1 to S5) within and in the vicinity of a streaming vortex.

Table 2: The classification of the particle diameters from this study.

	Vortex	S1	S2	S3	S4	S5
Device 1	V1 to V4	5 µm 1.1 µm 0.79 µm				0.49 µm 0.38 µm 0.31 µm
Device 2	V1 and V3	5 µm 1.1 µm			0.79 µm 0.49 µm	0.38 µm 0.31 µm
	V2		0.79 µm 0.49 µm	0.38 µm 0.31 µm		
Device 3	V1 and V3	5 µm	1.1 µm 0.79 µm		0.49 µm 0.38 µm 0.31 µm	
	V2			0.49 µm 0.38 µm 0.31 µm		
Device 4	V1	5 µm	1.1 µm			
	V2				0.79 µm 0.49 µm 0.38 µm 0.31 µm	
	V3		1.1 µm		0.79 µm 0.49 µm 0.38 µm 0.31 µm	

3.6 The feasibility of sub-micron particle separation using ASE

3.6.1 Separation of S1 and S4 particles

Theoretically, separating S1 and S4 particles would seem feasible since the former exists at pressure nodes and the latter at vortex centres. However, their locations coincide in almost all devices. Hence, separation is not possible.

3.6.2 Separation of S1 and S2 particles

Spatial distance between S1 and S2 particles was observed in Device 2 (V2), and Devices 3 and 4 (all vortices). In Device 2, the movement of particles in V2 showed that the focusing effect by particle inertia always drives the particles away from the vortex centre, which coincide with the pressure node. However, for a given particle size (e.g., 1.1 μm and 0.79 μm), most particles remain mixed in V1 and V3 as they belong to S1 and S4. The spatial distance between S1 and S2 particles can be used to separate 5 μm and 1.1 μm / 0.79 μm particles in Device 3 and 5 μm and 1.1 μm particles in Device 4. Yet, to facilitate particle separation, the design of the microchannel needs to be refined to reduce the number of particle lines.

3.6.3 Separation of S2 and S4 particles

The separation of S2 and S4 particles requires a channel height of at least $0.75\lambda_f$ (Devices 3 and 4). Device 3 can separate 1.1 μm / 0.79 μm particles and particles ≤ 0.49 μm, while Device 4 can separate 1.1 μm particles and particles ≤ 0.79 μm. The results show that for the studied devices, separation of sub-micron particles (in Device 3) using the focusing effects by particle inertia and shear gradient is feasible but difficult due to the small distance between particles and the number of particle lines. For SSAW devices with channel width less than λ_{SAW}, the diameter of a vortex is roughly equal to $\lambda_{SAW}/4$ [50]. Considering the vortex centre located in the middle of the vortex, the separation distance becomes $\lambda_{SAW}/8$. TSAW devices may be able to produce streaming vortices larger than λ_{SAW}. Nevertheless, further refinement on the microchannel's geometry is needed to enlarge the streaming vortices, thereby increasing the distance between the vortex centre and the region of low streaming velocity.

4. Conclusion

This study demonstrated the ASE-induced focusing effect by particle inertia, provided the classification of particle motion in the vicinity of streaming vortices, and evaluated the impact of microchannel height.

For the newly discovered focusing effect to occur, particles need to be small enough to avoid ARF and enter the streaming vortices, but large enough that the inertia force is adequate to drive them to the region of low streaming velocity. Generally, the particle motion in an acoustic field is size-dependent and classified as one of the following five categories:

S1: driven by ARF to pressure nodes.

S2: dominated by particle inertia, which is large enough to drive the particles from the vortices to regions of low streaming velocity.

(Particles in this category are subject to the ASE-induced focusing effect by the particle inertia)

S3: dominated by particle inertia, which is inadequate for detachment, leaving particles on the outer radius of the vortices.

S4: concentrated at the vortex centres by the shear-induced inward radial movement.

(Particles in this category are subject to the ASE-induced focusing effect by the shear gradient)

S5: small particles that are solely driven by the Stokes drag force.

The microchannel height plays an important role in the streaming velocity, thereby changing the sizes of the five categories (S1 to S5).

Finally, we evaluated the feasibility of sub-micron particle separation using the ASE-induced focusing effects. The spatial distances between S1/S2 and S2/S4 are shown, indicating that the focusing effect by particle inertia can separate sub-micron particles from micron particles, and also from other sub-micron particles. However, the studied devices involve too many particle lines, and the spatial distances are narrow. A microchannel that contains fewer but larger streaming vortices would enable sub-micron particle separation by ASE.

Author contributions

T.W.L. conceived the project. T.W.L. and T.T. fabricated the acoustofluidic devices and conducted the experiments. All authors discussed the results and contributed to the final manuscript. C.H.L. and C.Y.H.C supervised the project.

Declaration of competing interests

There are no conflicts to declare.

Acknowledgements

The funding for this research is provided by the Hong Kong Research Grant Council via the Hong Kong Ph.D. Fellowship Scheme (HKPFS) and the General Research Fund (GRF) projects (nos. 16206918, 17203220, & 17207121).

References

1 Y. Gao, M. Wu, Y. Lin, J. Xu, Acoustic microfluidic separation techniques and bioapplications: a review, Micromachines 11 (2020) 921.

2 M. Wu, A. Ozcelik, J. Rufo, Z. Wang, R. Fang, T.J. Huang, Acoustofluidic separation of cells and particles, Microsyst. Nanoeng. 5 (2019) 1-18.

3 S. Li, F. Ma, H. Bachman, C.E. Cameron, X. Zeng, T.J. Huang, Acoustofluidic bacteria separation, J. Micromech. Microeng. 27 (2016) 015031.

4 A. Shamloo, M. Boodaghi, Design and simulation of a microfluidic device for acoustic cell separation, Ultrasonics 84 (2018) 234-243.

5 Y. Chen, M. Wu, L. Ren, J. Liu, P.H. Whitley, L. Wang, T.J. Huang, High-throughput acoustic separation of platelets from whole blood, Lab Chip 16 (2016) 3466-3472.

6 J. Nam, H. Lim, D. Kim, S. Shin, Separation of platelets from whole blood using standing surface acoustic waves in a microchannel, Lab Chip 11 (2011) 3361-3364.

7 Z. Wang, H. Wang, R. Becker, J. Rufo, S. Yang, B.E. Mace, M. Wu, J. Zou, D.T. Laskowitz, T.J. Huang, Acoustofluidic separation enables early diagnosis of traumatic brain injury based on circulating exosomes, Microsyst. Nanoeng. 7 (2021) 1-11.

8 S. Li, X. Ding, Z. Mao, Y. Chen, N. Nama, F. Guo, P. Li, L. Wang, C.E. Cameron, T.J. Huang, Standing surface acoustic wave (SSAW)-based cell washing, Lab Chip 15 (2015) 331-338.

9 J.C. Hsu, C.H. Hsu, Y.W. Huang, Acoustophoretic control of microparticle transport using dual-wavelength surface acoustic wave devices, Micromachines 10 (2019) 52.

10 X. Ding, S.C.S. Lin, M.I. Lapsley, S. Li, X. Guo, C.Y. Chan, I.K. Chiang, L. Wang, J.P. McCoy, T.J. Huang, Standing surface acoustic wave (SSAW) based multichannel cell sorting, Lab Chip 12 (2012) 4228-4231.

11 J. Shi, H. Huang, Z. Stratton, Y. Huang, T.J. Huang, Continuous particle separation in a microfluidic channel via standing surface acoustic waves (SSAW), Lab Chip 9 (2009) 3354-3359.

12 F. Petersson, L. Åberg, A.M. Swärd-Nilsson, T. Laurell, Free flow acoustophoresis: microfluidic-based mode of particle and cell separation, Anal. Chem 79 (2007) 5117-5123.

13 P.B. Muller, R. Barnkob, M.J.H. Jensen, H. Bruus, A numerical study of microparticle acoustophoresis driven by acoustic radiation forces and streaming-induced drag forces, Lab Chip 12 (2012) 4617-4627.

14 J. Lei, P. Glynne-Jones, M. Hill, Acoustic streaming in the transducer plane in ultrasonic particle manipulation devices, Lab Chip 13 (2013) 2133-2143.

15 P. Hahn, I. Leibacher, T. Baasch, J. Dual, Numerical simulation of acoustofluidic manipulation by radiation forces and acoustic streaming for complex particles, Lab Chip 15 (2015) 4302-4313.

16 N. Korozlu, A. Biçer, D. Sayarcan, O.A. Kaya, A. Cicek, Acoustic sorting of airborne particles by a phononic crystal waveguide, Ultrasonics 124 (2022) 106777.

17 M. Wu, K. Chen, S. Yang, Z. Wang, P.H. Huang, J. Mai, Z.Y. Li, T.J. Huang, High-throughput cell focusing and separation via acoustofluidic tweezers. Lab Chip 18 (2018) 3003-3010.

18 R. Barnkob, P. Augustsson, T. Laurell, H. Bruus, Acoustic radiation-and streaming-induced microparticle velocities determined by microparticle image velocimetry in an ultrasound symmetry plane, Phys. Rev. E 86 (2012) 056307.

19 A.A. Doinikov, P. Thibault, P. Marmottant, Acoustic streaming induced by two orthogonal ultrasound standing waves in a microfluidic channel, Ultrasonics 87 (2018) 7-19.

20 J.S. Bach, H. Bruus, Suppression of acoustic streaming in shape-optimized channels, Phys. Rev. Lett. 124 (2020) 214501.

21 J.T. Karlsen, W. Qiu, P. Augustsson, H. Bruus, Acoustic streaming and its suppression in inhomogeneous fluids, Phys. Rev. Lett. 120 (2018) 054501.

22 A.L. Bernassau, P. Glynne-Jones, F. Gesellchen, M. Riehle, M. Hill, D.R.S. Cumming, Controlling acoustic streaming in an ultrasonic heptagonal tweezers with application to cell manipulation, Ultrasonics 54 (2014) 268-274.

23 S. Oberti, A. Neild, R. Quach, J. Dual, The use of acoustic radiation forces to position particles within fluid droplets, Ultrasonics 49 (2009) 47-52.

24 H. Li, J.R. Friend, L.Y. Yeo, Surface acoustic wave concentration of particle and bioparticle suspensions, Biomed. Microdevices 9 (2007) 647-656.

25 R. Shilton, M.K. Tan, L.Y. Yeo, J.R. Friend, Particle concentration and mixing in microdrops driven by focused surface acoustic waves, J. Appl. Phys. 104 (2008) 014910.

26 D.J. Collins, Z. Ma, Y. Ai, Highly localized acoustic streaming and size-selective submicrometer particle concentration using high frequency microscale focused acoustic fields. Anal. Chem. 88 (2016) 5513-5522.

27 D.J. Collins, Z. Ma, J. Han, Y. Ai, Continuous micro-vortex-based nanoparticle manipulation via focused surface acoustic waves, Lab Chip 17 (2017) 91-103.

28 D.J. Collins, B.L. Khoo, Z. Ma, A. Winkler, R. Weser, H. Schmidt, J. Han, Y. Ai, Selective particle and cell capture in a continuous flow using micro-vortex acoustic streaming, Lab Chip 17 (2017) 1769-1777.

29 M. Antfolk, P.B. Muller, P. Augustsson, H. Bruus, T. Laurell, Focusing of sub-micrometer particles and bacteria enabled by two-dimensional acoustophoresis, Lab Chip 14 (2014) 2791-2799.

30 P.R. Rogers, J.R. Friend, L.Y. Yeo, Exploitation of surface acoustic waves to drive size-dependent microparticle concentration within a droplet, Lab Chip 10 (2010) 2979-2985.

31 G. Guan, L. Wu, A.A. Bhagat, Z. Li, P.C. Chen, S. Chao, C.J. Ong, J. Han, Spiral microchannel with rectangular and trapezoidal cross-sections for size based particle separation, Sci Rep 3 (2013) 1475.

32 Y. Gou, Y. Jia, P. Wang, C. Sun, Progress of inertial microfluidics in principle and application, Sensors 18 (2018) 1762.

33 A. El Hasni, K. Göbbels, A.L. Thiebes, P. Bräunig, W. Mokwa, U. Schnakenberg, Focusing and sorting of particles in spiral microfluidic channels, Procedia Engineering 25 (2011) 1197-1200.

34 A.Y. Varaksin, S.V. Ryzhkov, Vortex Flows with Particles and Droplets (A Review), Symmetry 14 (2022) 2016.

35 T.W. Lai, S.C. Fu, K.C. Chan, C.Y.H. Chao, The use of acoustic streaming in Sub-micron particle sorting, Aerosol Science and Technology 56 (2022) 247-260.

36 M. Wiklund, R. Green, M. Ohlin, Acoustofluidics 14: Applications of acoustic streaming in microfluidic devices, Lab Chip 12 (2012) 2438-2451.

37 J. Wu, Acoustic streaming and its applications, Fluids 3 (2018) 108.

38 K. Kolesnik, P. Hashemzadeh, D. Peng, M.E.M. Stamp, W. Tong, V. Rajagopal, M. Miansari, D.J. Collins, Periodic Rayleigh streaming vortices and Eckart flow arising from traveling-wave-based diffractive acoustic fields, Phys. Rev. E 104 (2021) 045104.

39 J. Vanneste, O. Bühler, Streaming by leaky surface acoustic waves, Proc. R. Soc. A. 467 (2011) 1779-1800.

40 X. Ding, P. Li, S.C.S. Lin, Z.S. Stratton, N. Nama, F. Guo, D. Slotcavage, X. Mao, J. Shi, F. Costanzo, T.J. Huang, Surface acoustic wave microfluidics, Lab Chip 13 (2013) 3626-3649.

41 M. Alghane, B.X. Chen, Y.Q. Fu, Y. Li, J.K. Luo, A.J. Walton, Experimental and numerical investigation of acoustic streaming excited by using a surface acoustic wave device on a 128° YX-LiNbO3 substrate, J. Micromech. Microeng. 21 (2010) 015005.

42 K. Sritharan, C.J. Strobl, M.F. Schneider, A. Wixforth, Z.V. Guttenberg, Acoustic mixing at low Reynold's numbers, Appl. Phys. Lett. 88 (2006) 054102.

43 S. Shiokawa, Y. Matsui, T. Ueda, Study on SAW streaming and its application to fluid devices, Jpn. J. Appl. Phys. 29 (1990) 137.

44 S. Shiokawa and Y. Matsui, The dynamics of SAW streaming and its application to fluid devices, Mater. Res. Soc. Symp. Proc. 360 (1995) 53.

45 C. Devendran, T. Albrecht, J. Brenker, T. Alan, A. Neild, The importance of travelling wave components in standing surface acoustic wave (SSAW) systems, Lab Chip 16 (2016) 3756-3766.

46 C. Devendran, D.J. Collins, A. Neild, The role of channel height and actuation method on particle manipulation in surface acoustic wave (SAW)-driven microfluidic devices, Microfluid Nanofluid 26 (2022) 9.

47 A. Lenshof, M. Evander, T. Laurell, J. Nilsson, Acoustofluidics 5: Building microfluidic acoustic resonators, Lab Chip 12 (2012) 684-695.

48 S. Liu, Y. Yang, Z. Ni, X. Guo, L. Luo, J. Tu, D. Zhang, J. Zhang, Investigation into the effect of acoustic radiation force and acoustic streaming on particle patterning in acoustic standing wave fields, Sensors 17 (2017) 1664.

49 W. Guo, A.J.T. Teo, A.M. Gañán-Calvo, C. Song, N.T. Nguyen, H.D. Xi, S.H. Tan, Pressure-driven filling of closed-end microchannel: realization of comb-shaped transducers for acoustofluidics, Phys. Rev. Applied 10 (2018) 054045.

50 J. Dong, D. Liang, X. Yang, C. Sun, Influences of microparticle radius and microchannel height on SSAW-based acoustophoretic aggregation, Ultrasonics 117 (2021) 106547.

51 E. Taatizadeh, A. Dalili, P.I. Rellstab‐Sánchez, H. Tahmooressi, A. Ravishankara, N. Tasnim, H. Najjaran, I.T.S. Li, M. Hoorfar, Micron-sized particle separation with standing surface acoustic wave—Experimental and numerical approaches, Ultrason Sonochem 76 (2021) 105651.

(a) (b)

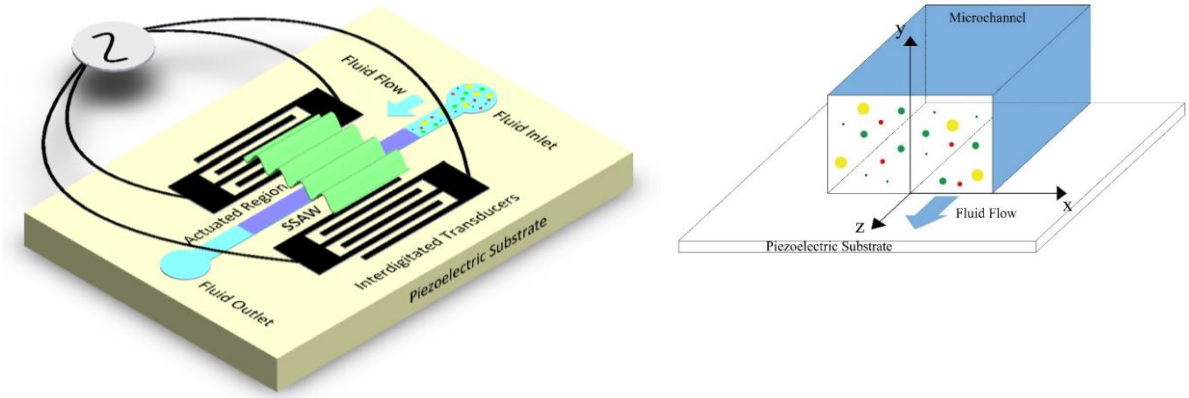

Figure 1: (a) The schematic diagram of SSAW devices. (b) The coordinate system employed in this study.

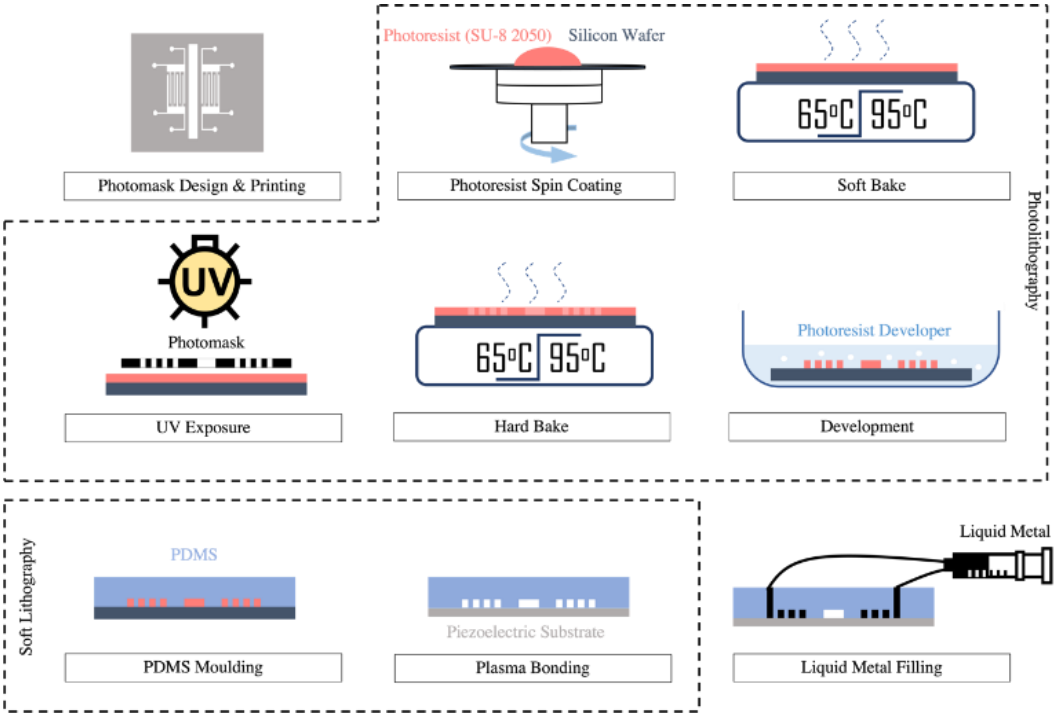

Figure 2: Fabrication process of the self-aligned IDT devices.

(a)

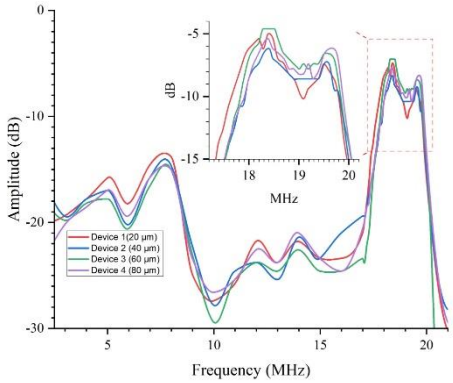

(b)

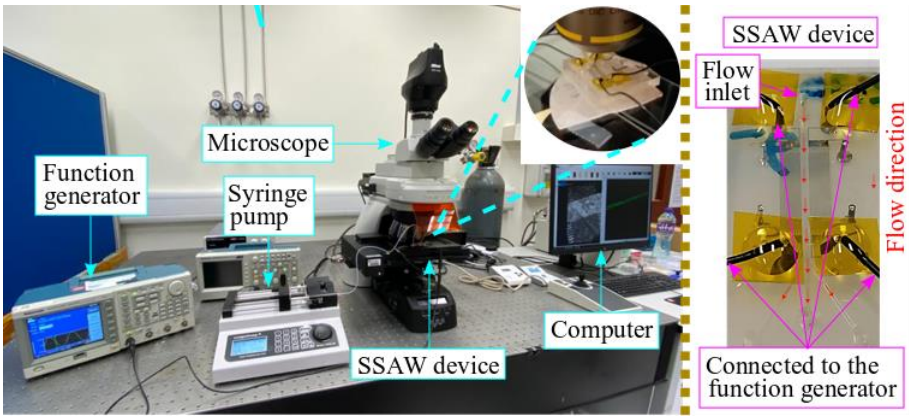

Figure 3: (a) Frequency response of Devices 1 to 4. (b) The experimental setup. The device was placed on the stage of the microscope. The inset image shows the device on the stage. The right image shows the device on which the red arrows indicate the flow direction.

a) b)

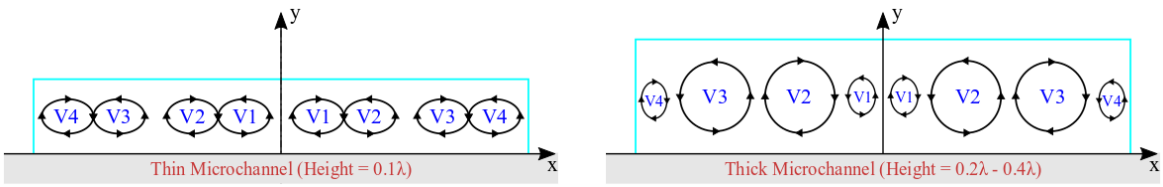

Figure 4: Schematic diagrams of the streaming pattern in the cross-sectional view of a) thin (Device 1), and b) thick (Devices 2-4) microchannels. The streaming vortices are identified as V1 to V4 from the y-axis to sidewalls.

(a) Device 1

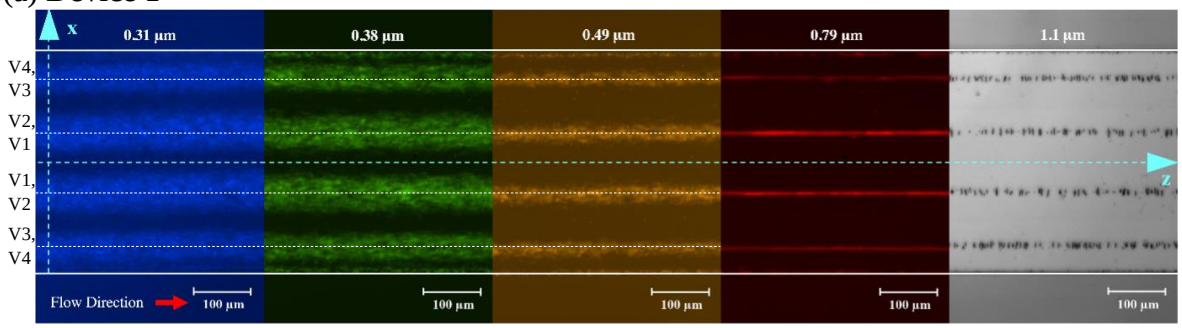

V1 to V4	V1 to V4	V1 to V4	Particles driven by ARF.	Particles driven by ARF.

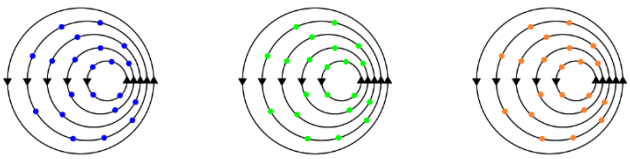

(b) Device 2

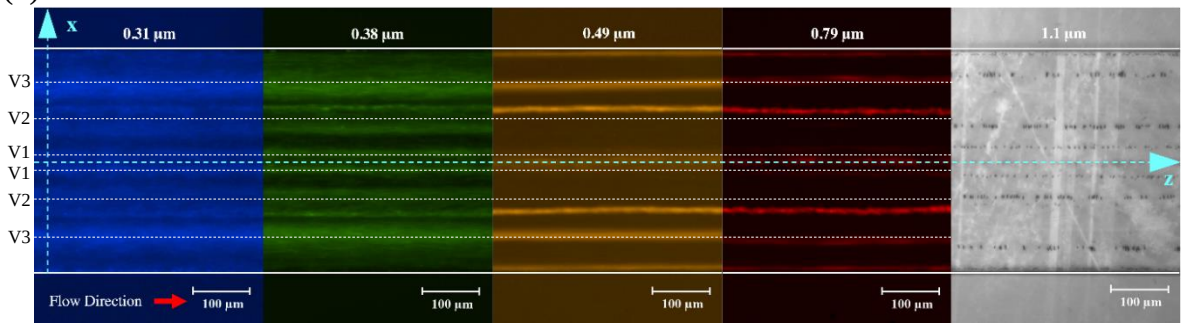

V1 and V3	V1 and V3	V1 and V3	V1 and V3	Particles driven by ARF.

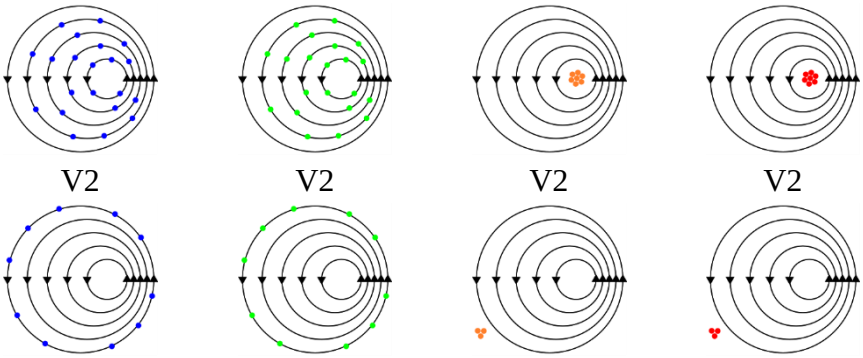

V2	V2	V2	V2

(c) Device 3

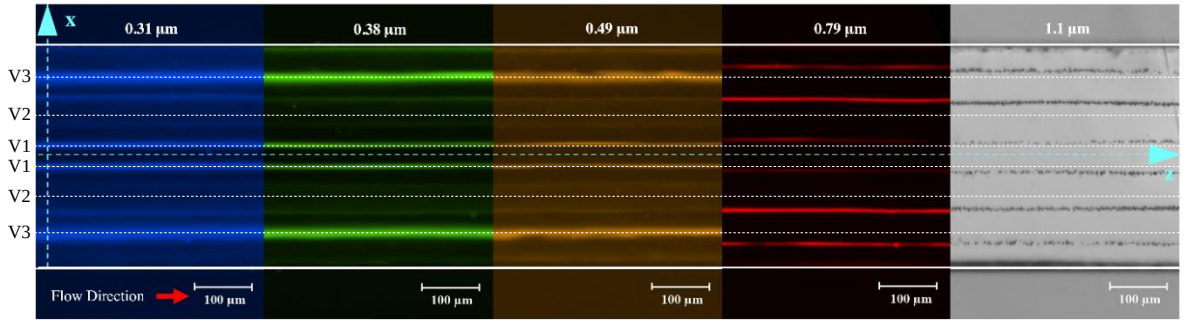

V1 and V3	V1 and V3	V1 and V3	V1 to V3	V1 to V3

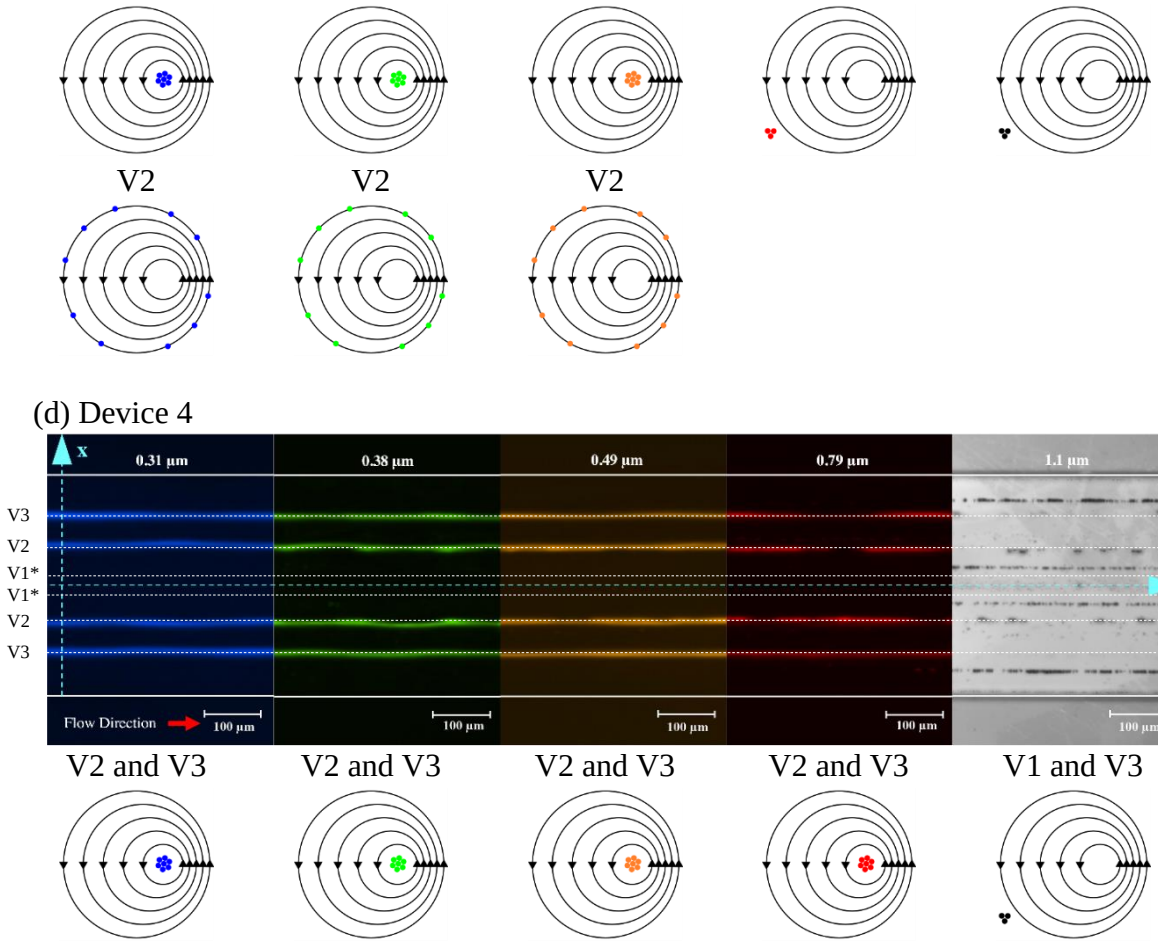

Figure 5: Distribution of 0.31 µm (blue), 0.38 µm (green), 0.49 µm (orange), 0.79 µm (red), and 1.1 µm (black) polystyrene particles in (a) Device 1, (b) Device 2, (c) Device 3, and (d) Device 4. Images show the top view of the microchannels. The flow direction is from left to right (positive z-direction). The channel walls are indicated by the white lines and the scale bar is 100 µm. The white dashed lines indicate the centre of the vortices. In (a), the centrelines of V1/V2 or V3/V4 are very close. In (d), the location of centreline of V1 (V1*) is estimated. The schematic diagrams below each image illustrate the location of the particles within and in the vicinity of streaming vortices.

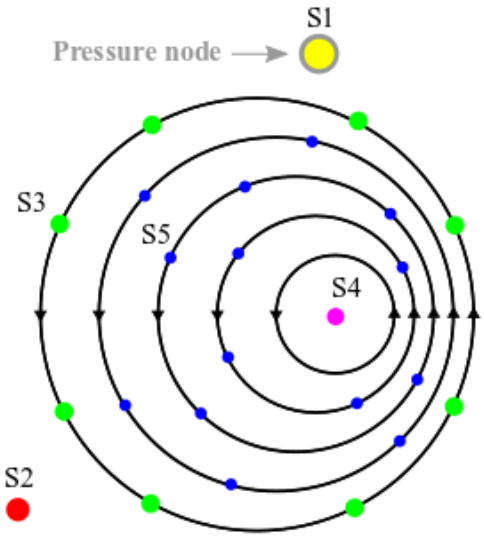

Figure 6: Schematic diagram showing the position of the size categories (S1 to S5) within and in the vicinity of a streaming vortex.

Table 1: X-position of the 5 μm Particles.

Device no.	Channel height (h)	x-position of the 5 μm particles (μm)				
1	$0.25\lambda_f$	±52	±149			
2	$0.5\lambda_f$	0	±25	±62	±150	±185
3	$0.75\lambda_f$	0	±60	±135	±185	
4	λ_f	0	±60	±127	±177	

Table 2: The classification of the particle diameters from this study.

	Vortex	S1	S2	S3	S4	S5
Device 1	V1 to V4	5 µm 1.1 µm 0.79 µm				0.49 µm 0.38 µm 0.31 µm
Device 2	V1 and V3	5 µm 1.1 µm			0.79 µm 0.49 µm	0.38 µm 0.31 µm
	V2		0.79 µm 0.49 µm	0.38 µm 0.31 µm		
Device 3	V1 and V3	5 µm	1.1 µm 0.79 µm		0.49 µm 0.38 µm 0.31 µm	
	V2			0.49 µm 0.38 µm 0.31 µm		
Device 4	V1	5 µm	1.1 µm			
	V2				0.79 µm 0.49 µm 0.38 µm 0.31 µm	
	V3		1.1 µm		0.79 µm 0.49 µm 0.38 µm 0.31 µm	